Basins and bifurcations of a delayed feedback control system and its experimental verification for a DC bus circuit

Noname manuscript No.
(will be inserted by the editor)

Basins and bifurcations of a delayed feedback control system and its experimental verification for a DC bus circuit

Koki Yoshida · Keiji Konishi · Naoyuki Hara

Received: date / Accepted: date

Abstract The present study deals with the basins of the equilibrium points embedded within the normal forms of Bogdanov-Takens bifurcation with delayed feedback control. It is numerically shown that the unstable periodic orbit that coexists with the equilibrium point stabilized by delayed feedback control is associated with the basin of the stabilized point. The relation between the periodic orbit and the basin indicates that for enlarging the basin, a homoclinic bifurcation for the orbit and a saddle point can provide useful information for the design of delayed feedback controllers. These results are experimentally confirmed in a real direct-current bus circuit that has dynamics similar to that of the normal form.

Keywords Basin · Bifurcation · Delayed feedback control · Direct-current bus circuit

1 Introduction

Nonlinear autonomous systems have limit sets, such as equilibrium points and periodic orbits. These limit sets are categorized as stable or unstable, for which the trajectories of the system converge to (diverge from) stable (unstable) limit sets. It is well known that an infinite number of unstable periodic orbits (UPOs) are embedded in a chaotic attractor of nonlinear systems. Several methods for controlling chaos, which stabilize UPOs or unstable equilibrium points embedded within a chaotic attractor, have been proposed for suppressing chaotic unpredictable behavior [2]. Delayed feedback control (DFC) [3], an attractive method for controlling chaos, has received considerable attention in terms of science and engineering applications. Because the control signal of DFC is proportional to the difference between the current system state and the delayed one, DFC has the following features: the control law does not require knowledge of the location of the target; a target state can be tracked even when the target location slowly changes; the control signal vanishes when the stabilization of target state is achieved. These features are of scientific and practical interest and thus numerous modifications and experimental implementations of DFC have been presented (for a review, see [4,5]).

The stability of periodic orbits or equilibrium points with DFC has been extensively investigated in the fields of nonlinear science [6–11] and control theory [12–15]. Most studies on stability have examined only the *local* stability of periodic orbits or equilibrium points using linear stability analysis. It is well accepted that delayed feedback controllers can be designed such that the periodic orbits or equilibrium points of nonlinear oscillators are locally stable [13–17]. A *global* stability analysis is necessary for elucidating the behavior of DFC systems far from the orbits or points. In particular, the basins of attraction, which can be obtained from a global stability analysis, provide useful information on the robustness of DFC systems against external disturbances. Hence, from a practical point of view, information on the basins in DFC systems is important for the design of delayed feedback controllers. However, it is not easy to handle the basins of DFC systems due to their initial conditions in *infinite*-dimensional phase space (see Appendix A). Thus, information on designing controllers to expand basins is limited.

This paper is a substantially extended version of a conference paper presented at the SICE Annual Conference 2018 [1].

K. Yoshida · K. Konishi (✉) · N. Hara
Department of Electrical and Information Systems, Osaka Prefecture University, 1-1 Gakuen-cho, Naka-ku, Sakai, Osaka 599-8531, Japan
E-mail: konishi@eis.osakafu-u.ac.jp

To reduce the infinite-dimensional initial conditions of time-delayed systems to *finite*-dimensional conditions, several studies have proposed restrictions for the phase space, such as those based on constant values [18], an equilibrium point [19], a history of uncontrolled dynamics [20–22], polynomial approximation [23], and a finite number of orthogonal basis functions [24,25]. These restrictions provide only partial information regarding basins[1]. Basins strongly depend on bifurcation scenarios in DFC systems. For the case where the target state is a periodic orbit, previous studies have reported analytical and experimental results on the relation of the basin to the super- and subcritical Hopf bifurcations of periodic orbits [21,26,27] (see Sec. 4 for more details). For the case where the target state is an equilibrium point, such a relation has rarely been investigated.

The present paper focuses on the basin of an equilibrium point in a DFC system. The relation between the partial information of the basin and a bifurcation scenario is investigated numerically. The DFC system consists of the normal form of Bogdanov-Takens bifurcation [28] and a simple delayed feedback controller. Note that this normal form has dynamics similar to that of a direct-current (DC) bus circuit [29–34], which has been extensively investigated as a fundamental circuit in the field of power electronics. The main contributions of the present paper are as follows: 1) it is shown that a UPO created by a subcritical Hopf bifurcation, which coexists with the equilibrium point stabilized with DFC, strongly depends on the size of the basin; 2) it is found that a homoclinic bifurcation for the UPO and a saddle point is important in the design of delayed feedback controllers that increase the size of the basin; 3) these numerical results are experimentally confirmed using a real DC bus circuit.

The rest of this paper is organized as follows. Section 2 describes the normal form of Bogdanov-Takens bifurcation with a simple delayed feedback controller. It is numerically shown that the size of the basin with three typical restricted initial conditions [18–22] increases with an increase in the size of the coexisting UPO. Further, it is shown that the homoclinic bifurcation curve in the control parameter space (i.e., feedback gain vs. delay time) divides the space into a region with a large basin and a region with a small basin. In Sec. 3, the results of Sec. 2 are numerically confirmed using a DC bus model with DFC. In addition, the size of the basin with three restricted initial conditions is experimentally investigated using a real DC bus circuit. Section 4 reviews related work. Finally, conclusions are given in Sec. 5.

[1] See Subsec. 2.2 for more details.

2 Normal form of Bogdanov-Takens bifurcation

This section investigates the bifurcations and basins of the normal form of Bogdanov-Takens bifurcation [28] with DFC.

2.1 Normal form with DFC

This subsection describes the normal form of Bogdanov-Takens bifurcation with DFC and analyzes its stability. The normal form [28] with DFC is given by

$$\begin{cases} \dot{x}_1(t) = x_2(t), \\ \dot{x}_2(t) = \beta_1 + \beta_2 x_1(t) + x_1(t)^2 + \alpha x_1(t) x_2(t) \\ \qquad\quad + k\left\{x_2(t-\tau) - x_2(t)\right\}. \end{cases} \tag{1}$$

System (1) has two variables, namely $x_1(t) \in \mathbb{R}$ and $x_2(t) \in \mathbb{R}$. Throughout this paper, the parameters β_1, β_2, and α are fixed as follows:

$$\beta_1 = 1/2, \quad \beta_2 = -2, \quad \alpha = 1. \tag{2}$$

For these parameters, a subcritical Hopf bifurcation and a homoclinic bifurcation, which play an important role in the basins of the DC bus circuit described in Sec. 3, occur in system (1). The term $k\left\{x_2(t-\tau) - x_2(t)\right\}$ in system (1) represents the control signal of DFC with feedback gain $k \in \mathbb{R}$ and delay time $\tau \geq 0$. This system has the following two equilibrium points:

$$\begin{aligned} [x_1, x_2]^{\mathrm{T}} &= [x_{1l}^*, x_{2l}^*]^{\mathrm{T}} = \left[1 - 1/\sqrt{2}, 0\right]^{\mathrm{T}}, \\ [x_1, x_2]^{\mathrm{T}} &= [x_{1r}^*, x_{2r}^*]^{\mathrm{T}} = \left[1 + 1/\sqrt{2}, 0\right]^{\mathrm{T}}. \end{aligned} \tag{3}$$

For $k = 0$ (i.e., without DFC), $[x_{1l}^*, x_{2l}^*]^{\mathrm{T}}$ is an unstable spiral point and $[x_{1r}^*, x_{2r}^*]^{\mathrm{T}}$ is a saddle point. Because the Jacobian matrix at the saddle point has one positive real eigenvalue, DFC never stabilizes the saddle point due to the well-known odd-number limitation [13,14]. This limitation guarantees that DFC never stabilizes the equilibrium point at which the Jacobian matrix has an odd number of real positive eigenvalues. Thus, in what follows, we deal with only the unstable spiral point $[x_{1l}^*, x_{2l}^*]^{\mathrm{T}}$ as the target equilibrium point.

To analyze the stability of this point, we investigate the linearized dynamics of system (1) at $[x_{1l}^*, x_{2l}^*]^{\mathrm{T}}$, expressed as

$$\begin{aligned} \begin{bmatrix} \delta\dot{x}_1(t) \\ \delta\dot{x}_2(t) \end{bmatrix} = \begin{bmatrix} 0 & 1 \\ -2 + 2x_{1l}^* & x_{1l}^* - k \end{bmatrix} \begin{bmatrix} \delta x_1(t) \\ \delta x_2(t) \end{bmatrix} \\ + \begin{bmatrix} 0 & 0 \\ 0 & k \end{bmatrix} \begin{bmatrix} \delta x_1(t-\tau) \\ \delta x_2(t-\tau) \end{bmatrix}, \end{aligned} \tag{4}$$

where $[\delta x_1, \delta x_2]^{\mathrm{T}} := [x_1, x_2]^{\mathrm{T}} - [x^*_{1l}, x^*_{2l}]^{\mathrm{T}}$ denotes the deviation from $[x^*_{1l}, x^*_{2l}]^{\mathrm{T}}$. The characteristic equation of system (4) is expressed as

$$g(\lambda, \tau) := \lambda^2 - \left\{x^*_{1l} - k(1 - e^{-\lambda\tau})\right\}\lambda + 2 - 2x^*_{1l} = 0. \quad (5)$$

Based on the results of a previous study [13] and Eq. (5), we can design the control parameters (k, τ) such that $[x^*_{1l}, x^*_{2l}]^{\mathrm{T}}$ is locally stable.

Theorem 1 *[13]*
Consider system (1) *with parameters* (2). *If k satisfies the inequalities,*

$$\begin{aligned} &c_1 := \left(-2 + \sqrt{2}\right)\left(\frac{6 + 9\sqrt{2}}{4} + k\right) < 0, \\ &c_2 := c_1^2 - 8 > 0, \\ &\phi_1/\omega_1 < \phi_2/\omega_2, \end{aligned} \quad (6)$$

where

$$\omega_1 := \sqrt{\frac{-c_1 - \sqrt{c_2}}{2}}, \quad \omega_2 := \sqrt{\frac{-c_1 + \sqrt{c_2}}{2}},$$

$$\phi_i := \mathrm{Arg}\left(\frac{j\omega_i k}{\sqrt{2} - \omega_i^2 + j\omega_i\left(k - 1 + 1/\sqrt{2}\right)}\right), \ i = 1, 2,$$

then $[x^*_{1l}, x^*_{2l}]^T$ is locally stable for τ belonging to

$$\begin{aligned} &\tau \in \left(\frac{\phi_1 + 2\pi l}{\omega_1}, \frac{\phi_2 + 2\pi l}{\omega_2}\right), \\ &l = 0, \ldots, \left\lfloor \frac{\phi_2\omega_1 - \phi_1\omega_2}{2\pi(\omega_2 - \omega_1)} \right\rfloor. \end{aligned} \quad (7)$$

$\lfloor y \rfloor$ indicates the largest integer that is not greater than $y \in \mathbb{R}$. $\mathrm{Arg}(z)$ is the argument of complex number z defined as $\mathrm{Arg}(z) \in [0, 2\pi)$.

The main result of the previous study [13] was to provide a design of the control parameters (k, τ) that stabilize linear systems with just two unstable modes. In contrast to the previous study, Theorem 1 considers only the two-dimensional unstable linearized system (4) (i.e., system (1) with fixed parameters (2) at the spiral point). The present paper deals with a specific case of the main result in [13].

Figure 1 shows the upper τ (black curves) and lower τ (red curves) given by Eq. (7). The shaded areas enclosed by these curves in k–τ space are the sets of (k, τ) for which $[x^*_{1l}, x^*_{2l}]^{\mathrm{T}}$ is locally stable. It should be mentioned that this theorem can provide information only on the local stability of $[x^*_{1l}, x^*_{2l}]^{\mathrm{T}}$ (i.e., not on its basin and global stability). The present paper demonstrates how to determine the control parameters (k, τ) within the stable sets.

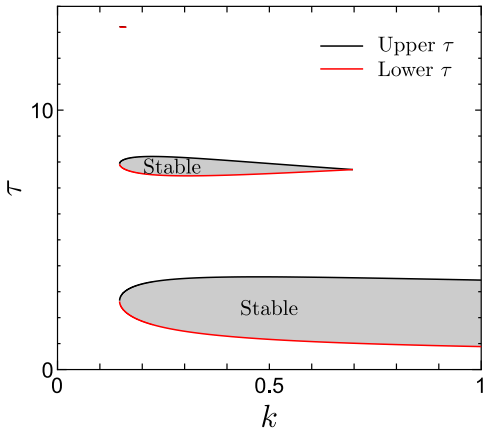

Fig. 1: Stability region of $[x^*_{1l}, x^*_{2l}]^{\mathrm{T}}$ of system (1) with parameters (2) in k–τ space.

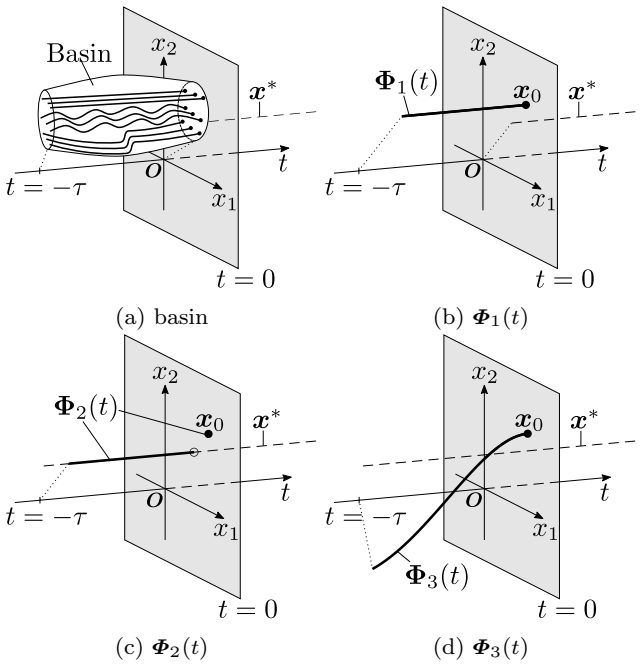

Fig. 2: Illustrations of (a) a basin of equilibrium point $\boldsymbol{x}^*$ and restricted initial functions (b) $\boldsymbol{\Phi}_1(t)$, (c) $\boldsymbol{\Phi}_2(t)$, and (d) $\boldsymbol{\Phi}_3(t)$, which are defined in Eqs. (8)–(10), respectively.

2.2 Basins with three restricted initial functions

This subsection numerically evaluates the size of the basin of $[x^*_{1l}, x^*_{2l}]^{\mathrm{T}}$ in system (1). A basin is a set of initial conditions for which the trajectories converge to the target equilibrium point. It is well known that for dynamical systems that include time delays, the basin is a set of time functions (i.e., initial functions), as sketched in Fig. 2(a). In other words, the basin is described by initial points in infinite-dimensional phase

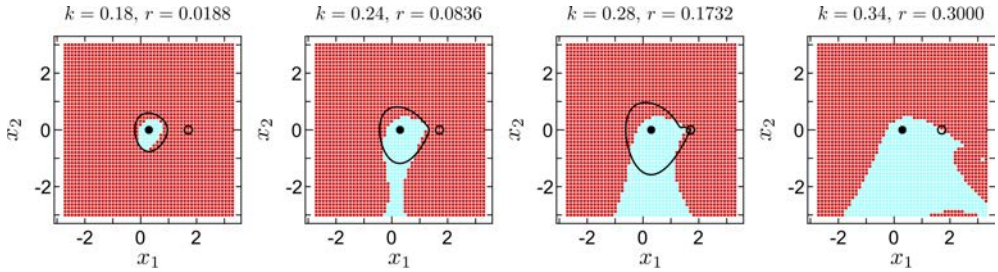

(a) with $\boldsymbol{\Phi}_1(t)$

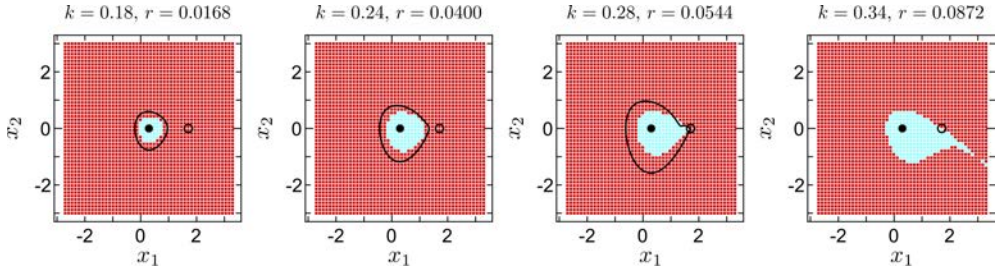

(b) with $\boldsymbol{\Phi}_2(t)$

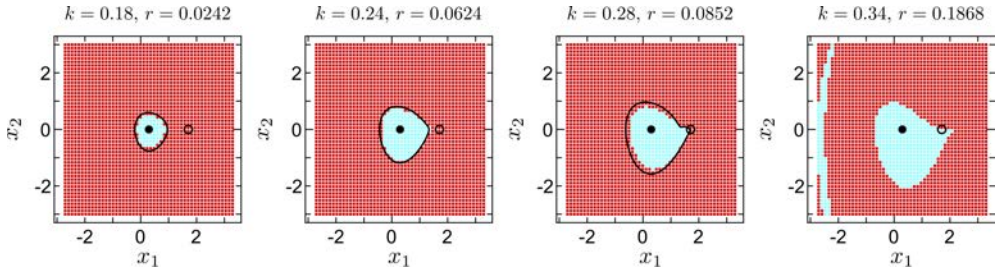

(c) with $\boldsymbol{\Phi}_3(t)$

Fig. 3: Basins of $[x_{1l}^*, x_{2l}^*]^{\mathrm{T}}$ in system (1) with parameters (2) for $\tau = 3.0$. Sets of initial states $\boldsymbol{x}_0$ for (a) $\boldsymbol{\Phi}_1(t)$, (b) $\boldsymbol{\Phi}_2(t)$, and (c) $\boldsymbol{\Phi}_3(t)$. Light-blue and red dots respectively indicate those for which trajectories converge and do not converge on $[x_{1l}^*, x_{2l}^*]^{\mathrm{T}}$. Black lines around $[x_{1l}^*, x_{2l}^*]^{\mathrm{T}}$ are trajectories of UPOs. Closed and open circles indicate equilibrium points $[x_{1l}^*, x_{2l}^*]^{\mathrm{T}}$ and $[x_{1r}^*, x_{2r}^*]^{\mathrm{T}}$, respectively.

space. Thus, it is quite difficult to visualize and determine the basin of time-delayed systems. To deal with such basins, the present study evaluates the basin of $[x_{1l}^*, x_{2l}^*]^{\mathrm{T}}$ with three types of restricted initial function used in previous studies [18–22] (see Figs. 2(b)–2(d)).

Definition 1 The initial functions $\boldsymbol{\Phi}_{1,2,3}(t) : \mathbb{R} \to \mathbb{R}^2$ are respectively defined as

$$\boldsymbol{\Phi}_1(t) := \boldsymbol{x}_0,\ t \in [-\tau, 0]\,, \tag{8}$$

$$\boldsymbol{\Phi}_2(t) := \begin{cases} \boldsymbol{x}^*, & t \in [-\tau, 0) \\ \boldsymbol{x}_0, & t = 0 \end{cases}, \tag{9}$$

$$\boldsymbol{\Phi}_3(t) := \boldsymbol{\Psi}(t, \boldsymbol{x}_0),\ t \in [-\tau, 0]\,, \tag{10}$$

where $\boldsymbol{x}_0 := \boldsymbol{x}(0) \in \mathbb{R}^2$ is the state at time $t = 0$, $\boldsymbol{x}^*$ is the equilibrium point of system (1), and $\boldsymbol{\Psi} : \mathbb{R} \times \mathbb{R}^2 \to \mathbb{R}^2$ is the trajectory of system (1) without control (i.e., $k = 0$) passing through the state $\boldsymbol{x}(0) = \boldsymbol{x}_0$.

The present paper employs these three initial functions [18–22] because they each represent an actual situation in practical systems with DFC. Figures 2(b)–2(d) show the initial functions $\boldsymbol{\Phi}_1(t)$ [18], $\boldsymbol{\Phi}_2(t)$ [19], and $\boldsymbol{\Phi}_3(t)$ [20–22], respectively. $\boldsymbol{\Phi}_1(t)$ corresponds to the situation where the equilibrium point jumps from $\boldsymbol{x}_0$ to $\boldsymbol{x}^*$ due to a sudden change of a system parameter at $t = 0$, where $\boldsymbol{x}_0$ and $\boldsymbol{x}^*$ are the equilibrium points before and after the change, respectively. For $\boldsymbol{\Phi}_2(t)$, the state of the system on the stable equilibrium point $\boldsymbol{x}^*$ jumps to $\boldsymbol{x}_0$ due to an impulsive disturbance at $t = 0$. For $\boldsymbol{\Phi}_3(t)$, DFC starts to work at $t = 0$ in system (1) operating without control. Note that for a given state $\boldsymbol{x}_0$, there exist unique initial functions $\boldsymbol{\Phi}_1(t)$, $\boldsymbol{\Phi}_2(t)$, and $\boldsymbol{\Phi}_3(t)$. As a result, the basin of system (1), which is the set of initial functions, can be approximately evaluated by the sets of $\boldsymbol{x}_0$. Strictly speaking, each set of $\boldsymbol{x}_0$ is a subset of the basin. Although such subsets provide only par-

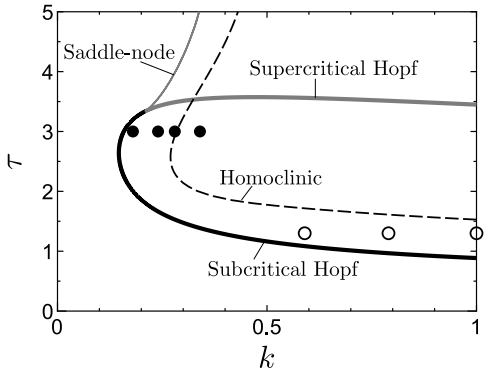

Fig. 4: Bifurcation curves of system (1) with parameters (2) in k–τ space. Closed and open circles represent parameters (k, τ) used in Figs. 3 and 5, respectively.

tial information regarding the basin, they can be used to visualize this information in finite-dimensional phase space. The finite-dimensional information can be easily visualized and understood.

We now numerically evaluate the basins with the initial functions $\boldsymbol{\Phi}_{1,2,3}(t)$. Figures 3(a)–3(c) show the basins (i.e., the sets of $\boldsymbol{x}_0$) with $\boldsymbol{\Phi}_1(t)$, $\boldsymbol{\Phi}_2(t)$, and $\boldsymbol{\Phi}_3(t)$, respectively. The delay time is fixed at $\tau = 3.0$ and the feedback gain is set to $k = 0.18$, 0.24, 0.28, and 0.34. The closed and open circles indicate the equilibrium points $[x_{1l}^*, x_{2l}^*]^{\mathrm{T}}$ and $[x_{1r}^*, x_{2r}^*]^{\mathrm{T}}$, respectively. The black lines around $[x_{1l}^*, x_{2l}^*]^{\mathrm{T}}$ represent the UPOs. The trajectories of system (1) with $\boldsymbol{x}_0 = [x_1(0), x_2(0)]^{\mathrm{T}}$ at the light-blue (red) dots[2] converge (do not converge) to $[x_{1l}^*, x_{2l}^*]^{\mathrm{T}}$.

To estimate the size of the basin, the index

$$r := \frac{\text{Size of basin}}{\text{Size of space } (x_1(0), x_2(0))}, \tag{11}$$

is introduced[3]. This index indicates the size ratio of the basin. It can be seen from Fig. 3 that the sizes of the UPO and of the basin increase with an increase in feedback gain k for all $\boldsymbol{\Phi}_{1,2,3}(t)$. In addition, the UPO merges with the saddle point $[x_{1r}^*, x_{2r}^*]^{\mathrm{T}}$ and disappears via a homoclinic bifurcation at $k \approx 0.28$. It should be noted that the boundaries of the basins with $\boldsymbol{\Phi}_3(t)$ are close to the UPOs (see Fig. 3(c)). This observation implies that the basins strongly depend on the UPOs; this dependence is numerically and experimentally investigated later. Further, from Fig. 3 with $k = 0.34$, we see that the basins are large even after the UPO disappears.

[2] The states $\boldsymbol{x}_0$ are set in 50×50 grids with $x_1(0) \in [x_{1l}^* - 3, x_{1l}^* + 3]$ and $x_2(0) \in [x_{2l}^* - 3, x_{2l}^* + 3]$. A light-blue (red) dot is plotted if the trajectory starting from the dot converges (does not converge) to $[x_{1l}^*, x_{2l}^*]^{\mathrm{T}}$. The criterion for the convergence is given by the inequality $\left|[x_1(1000) - x_{1l}^*, x_2(1000) - x_{2l}^*]^{\mathrm{T}}\right| < 0.01$.

[3] r is numerically obtained as (number of light-blue dots)/2500. The present paper deals with the largest set.

At this stage, it must be emphasized that if we want to determine the control parameters (k, τ) such that the basins are large, we have to numerically calculate a number of basins for a variety of parameters and restrictions, as done in Fig. 3. This calculation is not practical due to its heavy computation load. Therefore, we now turn our attention to the bifurcation of UPOs to easily determine the parameters.

2.3 Bifurcation curves and basins

To determine the relationship between the control parameters (k, τ) and the size of the basin, we numerically investigate the bifurcations of system (1) in k–τ space. The bifurcation curves are plotted in Fig. 4; they were obtained with the aid of the software DDE-BIFTOOL [35]. The thick black and thick gray curves represent the sub- and supercritical Hopf bifurcations, respectively. These curves are equivalent to the upper and lower τ given by Eq. (7) (see Fig. 1). The area enclosed by these curves is the stability region[4]. The thin gray curve represents the saddle-node bifurcation of periodic orbits. The broken curve shows the homoclinic bifurcation.

As can be seen from Fig. 4, with an increase in k from 0 for delay time $\tau \in [0.89, 3.33]$ ($\tau \in [3.34, 3.57]$), the unstable spiral point $[x_{1l}^*, x_{2l}^*]^{\mathrm{T}}$ is stabilized via a subcritical (supercritical) Hopf bifurcation. Here, we focus on the homoclinic bifurcation with an increase in k for two cases, namely $\tau = 3.0$ and $\tau = 1.3$. For $\tau = 3.0$ (see the closed circles in Fig. 4), the homoclinic bifurcation occurs at $k \approx 0.28$. In contrast, for $\tau = 1.3$ (see the open circles in Fig. 4), the homoclinic bifurcation does not occur for any $k \in [0, 1]$. The UPOs and the basins with $\boldsymbol{\Phi}_{1,2,3}(t)$ for $\tau = 1.3$ and $k = 0.59$, 0.79, and 1.00 are shown in Figs. 5(a)–5(c). Note that the closed (open) circles in Fig. 4 correspond to the control parameters (k, τ) in Fig. 3 (Fig. 5). As shown in Fig. 5, for $\tau = 1.3$, the sizes of the UPO and the basin increase with an increase in k; however, the rate of increase is lower than that for $\tau = 3.0$ (see Fig. 3).

We examine the relationship between the size of basins and the bifurcation curves using numerical simulations. The contours of the index r with $\boldsymbol{\Phi}_1(t)$, $\boldsymbol{\Phi}_2(t)$, and $\boldsymbol{\Phi}_3(t)$ are respectively plotted on the bifurcation curves in k–τ space in Figs. 6(a)–6(c). We now discuss the bifurcation scenario and the index r with an increase in k. Here, we focus on the index r with $\boldsymbol{\Phi}_3(t)$ shown in Fig. 6(c). For $\tau \in [3.34, 3.57]$, a supercritical Hopf bifurcation occurs with an increase in k; just after the bifurcation, r jumps to 0.05. In contrast, for

[4] The stability region shown in Fig. 1 has three stable sets.

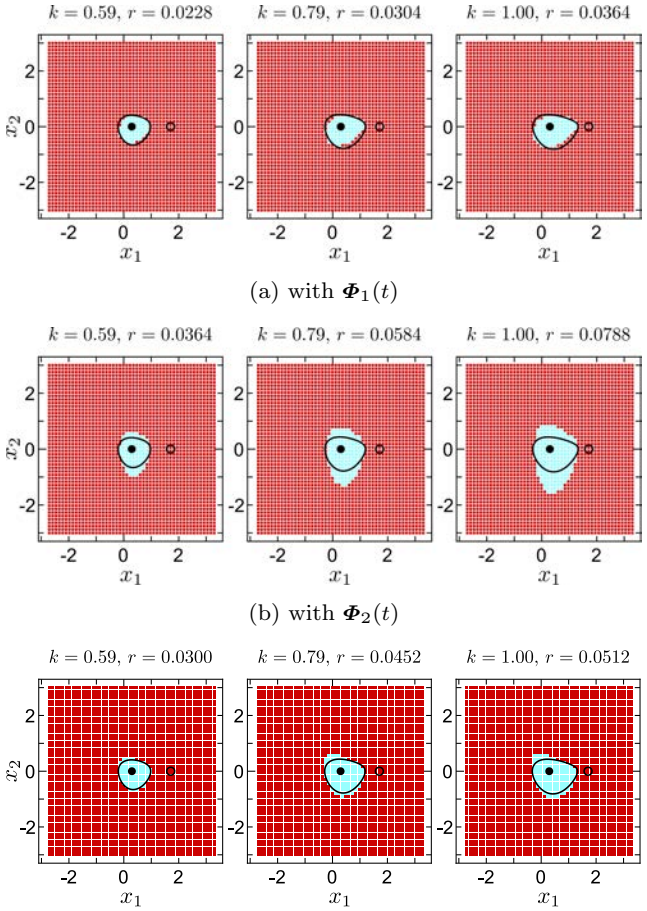

(a) with $\boldsymbol{\Phi}_1(t)$

(b) with $\boldsymbol{\Phi}_2(t)$

(c) with $\boldsymbol{\Phi}_3(t)$

Fig. 5: Basins of $[x^*_{1l}, x^*_{2l}]^{\mathrm{T}}$ in system (1) with parameters (2) for $\tau = 1.3$. Sets of initial states $\boldsymbol{x}_0$ for (a) $\boldsymbol{\Phi}_1(t)$, (b) $\boldsymbol{\Phi}_2(t)$, and (c) $\boldsymbol{\Phi}_3(t)$. Light-blue and red dots respectively indicate those for which trajectories converge and do not converge on $[x^*_{1l}, x^*_{2l}]^{\mathrm{T}}$. Black lines around $[x^*_{1l}, x^*_{2l}]^{\mathrm{T}}$ are trajectories of UPOs. Closed and open circles indicate equilibrium points $[x^*_{1l}, x^*_{2l}]^{\mathrm{T}}$ and $[x^*_{1r}, x^*_{2r}]^{\mathrm{T}}$, respectively.

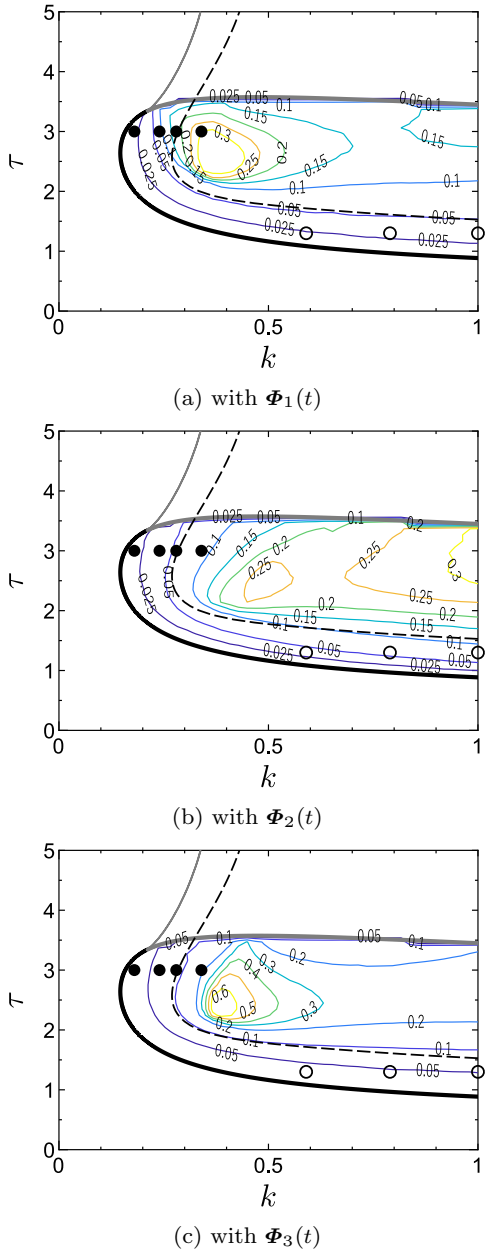

(a) with $\boldsymbol{\Phi}_1(t)$

(b) with $\boldsymbol{\Phi}_2(t)$

(c) with $\boldsymbol{\Phi}_3(t)$

Fig. 6: Contours of index r defined in Eq. (11) and bifurcation curves of system (1) with parameters (2) in k–τ space for (a) $\boldsymbol{\Phi}_1(t)$, (b) $\boldsymbol{\Phi}_2(t)$, and (c) $\boldsymbol{\Phi}_3(t)$.

$\tau \in [0.89, 3.33]$, a subcritical Hopf bifurcation occurs with an increase in k; just after the bifurcation, r gradually increases with k. This contrast is consistent with previous studies on the basins of periodic orbits [21, 26, 27]. A further increase in k for $\tau \in [1.54, 3.53]$ causes a homoclinic bifurcation. Note that the homoclinic bifurcation curve mostly follows the contour line of $r = 0.1$.

These properties also hold for Figs. 6(a) and 6(b). It can be concluded from these properties that the homoclinic bifurcation curve divides the control parameters (k, τ) space into a region with a large basin (i.e., right-hand side of the curve) and a region with a small basin (i.e., left-hand side of the curve). As a result, the homoclinic bifurcation curve can be used to design control parameters that make the basin large.

Let us now summarize the procedure for designing the control parameters.

1. We plot a stability region of the target equilibrium point in k–τ space using Theorem 1, as shown in Fig. 1.
2. We numerically plot a homoclinic bifurcation curve with the aid of the software DDE-BIFTOOL.

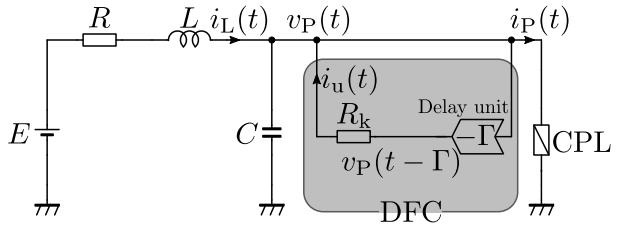

Fig. 7: Fundamental DC bus circuit with DFC. The delayed feedback controller, represented by the shaded area, consists of a delay unit and feedback resistor R_k. Voltage $v_P(t-\Gamma)$ with delay time $\Gamma \geq 0$ is applied to feedback resistor R_k. Control current $i_u(t)$ is injected into the bus circuit.

3. We choose the control parameters that are within the stability region and are located on the right-hand side of the homoclinic bifurcation curve.

This design procedure has a light computation load, which is its main advantage.

3 DC bus circuit

This section deals with the basin of an operating point of a DC bus system. The effectiveness of the parameter design based on the numerical bifurcation analysis in the preceding section is experimentally confirmed using a DC bus circuit.

3.1 Circuit model and bifurcations

DC bus systems are attractive for next-generation power systems because of their simple control, easy integration, high efficiency, and high reliability [36–40]. However, their voltage instability, which is induced by constant power loads (CPLs) that have regulated voltage converters, is still a challenge. Many studies in the field of power electronics have attempted to overcome this instability (see review articles [29–33] and a book [34]). Our previous study [41] reported the stabilization of a DC bus circuit with DFC. The stabilization was confirmed by circuit experiments [42]. One of our other studies extended the stabilization with DFC to a DC bus network [43].

Figure 7 shows a fundamental DC bus circuit with DFC [41,42]. E represents the voltage source. R, L, and C respectively denote the equivalent resistance, inductance, and capacitance in power lines and converters. The line current $i_L(t)$ and the supplied voltage $v_P(t)$ are the circuit variables at time t. The CPL consumes constant power P independent of $v_P(t)$; thus, the current through the CPL is given by

$$i_P(t) = P/v_P(t). \tag{12}$$

The delayed feedback controller, the shaded area in Fig. 7, consists of a delay unit and feedback resistor R_k. Voltage $v_P(t)$ is measured and previous voltage $v_P(t-\Gamma)$ with delay time $\Gamma \geq 0$ is applied to feedback resistor R_k. Control current $i_u(t)$ is proportional to the difference between current voltage $v_P(t)$ and previous voltage $v_P(t-\Gamma)$:

$$i_u(t) = \frac{1}{R_k}\{v_P(t-\Gamma) - v_P(t)\}. \tag{13}$$

The circuit variables and parameters are transformed as

$$\begin{aligned} &x_1 := \frac{1}{E}v_P, \quad x_2 := \frac{L}{RCE}i_L, \\ &a := \frac{RP}{E^2}, \quad b := \frac{R^2C}{L}, \quad k := \frac{R}{R_k}, \quad \tau := \frac{\Gamma}{RC}. \end{aligned} \tag{14}$$

Then, the dynamics of the DC bus circuit with DFC is rewritten as

$$\begin{cases} \dot{x}_1(t) = -\dfrac{a}{x_1(t)} + bx_2(t) + k\left\{x_1(t-\tau) - x_1(t)\right\}, \\ \dot{x}_2(t) = -x_1(t) - bx_2(t) + 1, \end{cases} \tag{15}$$

where dimensionless time t represents $t/(RC)$ of real time t. For $a < 0.25$, the DC bus circuit without DFC has the two equilibrium points $[x^*_{1\pm}, x^*_{2\pm}]^{\mathrm{T}}$ with

$$x^*_{1\pm} := \frac{1}{2}\left(1 \pm \sqrt{1-4a}\right), \quad x^*_{2\pm} := \frac{1}{b}\left(1 - x^*_{1\pm}\right). \tag{16}$$

The unstable spiral point $[x^*_{1+}, x^*_{2+}]^{\mathrm{T}}$ is the operating point of the DC bus circuit [41,42]. The saddle point $[x^*_{1-}, x^*_{2-}]^{\mathrm{T}}$ cannot be stabilized with DFC due to the odd-number limitation. In what follows, the parameters a and b are fixed to

$$a = 0.189, \quad b = 0.205. \tag{17}$$

The equilibrium points and the nullclines of system (15) without control are shown in Fig. 8. The dotted and solid lines are the nullclines of $\dot{x}_1 = 0$ and $\dot{x}_2 = 0$, respectively. The closed and open circles at the intersections of the nullclines are $[x^*_{1+}, x^*_{2+}]^{\mathrm{T}}$ and $[x^*_{1-}, x^*_{2-}]^{\mathrm{T}}$, respectively. It should be noted that our previous study [41] analytically provided the boundary curves of stability regions in k–τ space.

Figure 9 shows the bifurcation curves in k–τ space. The thick solid line denotes the subcritical Hopf bifurcation curve, which is the boundary obtained in our previous study [41]. The broken line is the homoclinic bifurcation curve, where a UPO around $[x^*_{1+}, x^*_{2+}]^{\mathrm{T}}$ merges

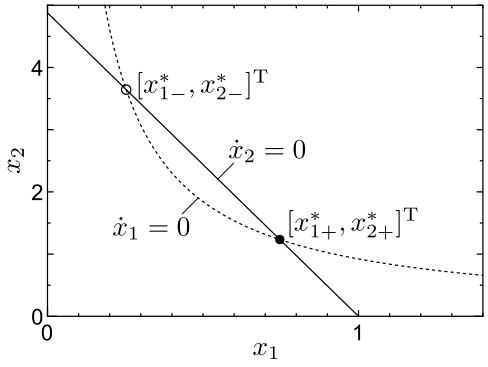

Fig. 8: Equilibrium points and nullclines of system (15) with $k = 0$, $a = 0.189$, and $b = 0.205$.

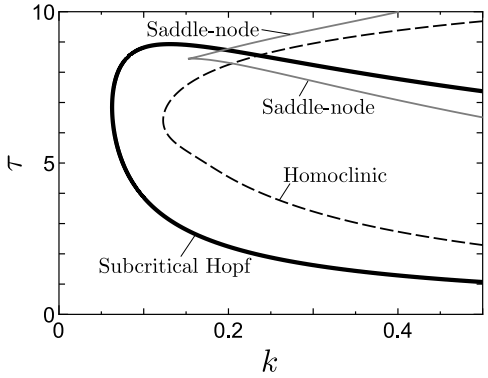

Fig. 9: Bifurcation curves of system (15) in k–τ space with $a = 0.189$ and $b = 0.205$.

with the saddle point $[x^*_{1-}, x^*_{2-}]^{\mathrm{T}}$. The gray line in Fig. 9 is explained in Appendix B. We see that the supercritical Hopf bifurcation that occurs in system (1) does not occur in system (15). With an increase in k from 0 for $\tau \in [1.07, 8.92]$, $[x^*_{1+}, x^*_{2+}]^{\mathrm{T}}$ is stabilized via a subcritical Hopf bifurcation. A further increase in k for $\tau \in [2.33, 8.53]$ causes a homoclinic bifurcation.

We now numerically evaluate the basin of $[x^*_{1+}, x^*_{2+}]^{\mathrm{T}}$ with $\boldsymbol{\Phi}_{1,2,3}(t)$[5]. Figures 10(a)–10(c) show the contours[6] of the index r and the bifurcation curves in k–τ space. As can be seen, the following property of the DC bus system (15) is similar to that of system (1): the homoclinic bifurcation curve divides the control parameter (k, τ) space into a region with a large basin and a region with a small basin.

[5] Although the functions described by Eqs. (8)–(10) are defined with respect to system (1), this section uses them with respect to system (15) instead of system (1).

[6] The numerical procedure used for calculating the index is the same as that for Fig. 6. The states $\boldsymbol{x}_0$ are set in 50×50 grids with $x_1(0) \in [0.1, 1.2]$ and $x_2(0) \in [0.1, 10]$.

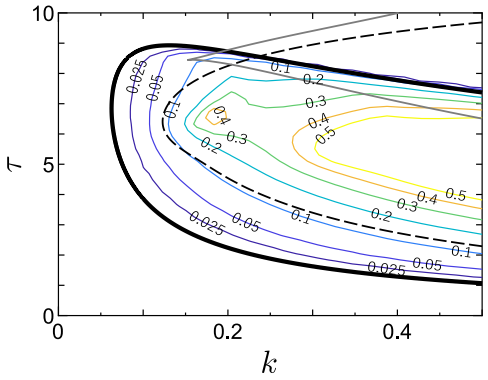

(a) with $\boldsymbol{\Phi}_1(t)$

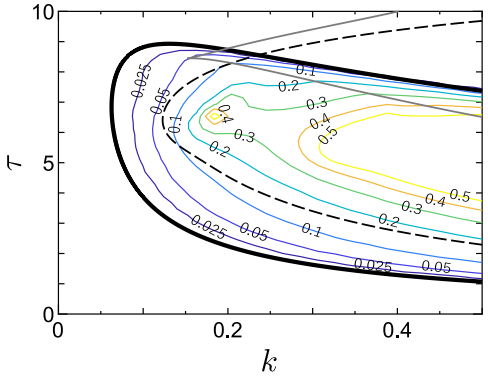

(b) with $\boldsymbol{\Phi}_2(t)$

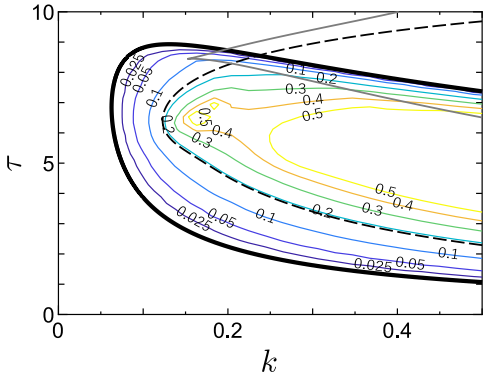

(c) with $\boldsymbol{\Phi}_3(t)$

Fig. 10: Contours of index r defined in Eq. (11) and bifurcation curves of system (15) with $a = 0.189$ and $b = 0.205$ in k–τ space for (a) $\boldsymbol{\Phi}_1(t)$, (b) $\boldsymbol{\Phi}_2(t)$, and (c) $\boldsymbol{\Phi}_3(t)$.

3.2 Circuit experiments

In this subsection, the numerical results of the preceding subsection are experimentally confirmed using a real DC bus circuit. The experimental setup of the DC bus circuit with DFC in Fig. 7, which was used in our previous study [42], is shown in Fig. 11. The circuit parameters are set to $E = 16.0$ V, $R = 22.8$ Ω,

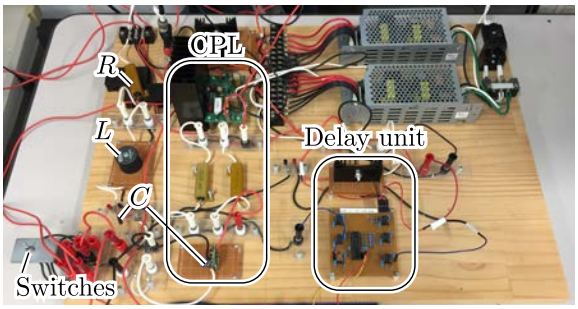

Fig. 11: Experimental setup of the DC bus circuit and a delayed feedback controller.

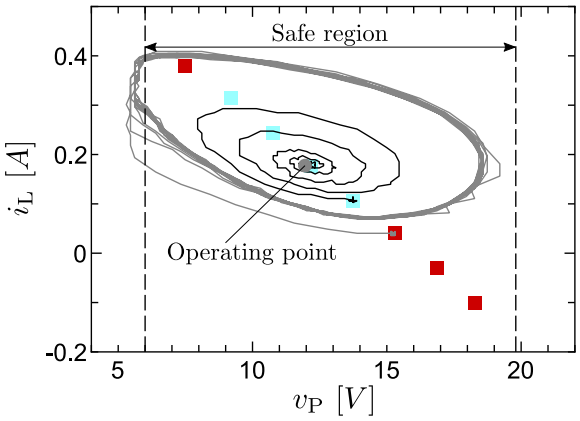

Fig. 12: Trajectories of the DC bus circuit from two initial points with $\boldsymbol{\Phi}_1(t)$ for $(k, \tau) = (0.12, 4.5)$. Trajectories from light-blue and red squares converge and do not converge on the operating point, respectively.

$L = 22.6$ mH, $C = 8.93$ μF, and $P = 2.12$ W, which correspond to the dimensionless parameters (17) used in the preceding subsection. The details of the circuit and the procedure used for setting the initial functions on the real circuit are described in Appendix C. The procedure allows us to set the initial points $v_{\mathrm{P}}(0)$ and $i_{\mathrm{L}}(0)$ on the line $i_L(0) = \{E - v_{\mathrm{P}}(0)\}/R$.

The DC bus circuit with DFC can work only for $v_{\mathrm{P}}(t) \in [6.0, 19.8]$ V due to the limited operating voltage range of the CPL and the controller. Here, *safe operation* is defined as follows: the voltage $v_{\mathrm{P}}(t)$ from an initial point converges to the equilibrium point without touching the edges of the range $v_{\mathrm{P}} \in [6.0, 19.8]$ V (see the broken lines in Fig. 12). The set of initial points for safe operation[7] is now defined as the basin of the equilibrium point.

The trajectories from the two initial points $[v_{\mathrm{P}}(0), i_{\mathrm{L}}(0)]^{\mathrm{T}} = [13.7\ \mathrm{V}, 0.10\ \mathrm{A}]^{\mathrm{T}}$ and $[15.2\ \mathrm{V}, 0.04\ \mathrm{A}]^{\mathrm{T}}$ with $\boldsymbol{\Phi}_1(t)$ in v_{P}–i_{L} space are shown in Fig. 12. The squares denote the following eight initial points:

$$v_{\mathrm{P}}(0) \in \{7.6, 9.1, 10.7, 12.2, 13.7, 15.2, 16.8, 18.3\}\ \mathrm{V}. \tag{18}$$

Safe operation was (was not) experimentally demonstrated at the light-blue (red) squares. The gray trajectory from the red square touches the edge of the safe range and then does not converge on the equilibrium point (i.e., the operating point). In contrast, the black trajectory from the light-blue square does not touch the edge and eventually converges on the point.

The time series with the control parameters on the left- and right-hand sides of the homoclinic bifurcation curve are shown in Figs. 13(a) and 13(b), respectively. The control parameters are fixed at $(R_{\mathrm{k}}, \Gamma) = (95\ \Omega, 0.500\ \mathrm{ms})$ $\big($i.e., $(k, \tau) = (0.24, 2.5)\big)$ for Fig. 13(a); they are fixed at $(R_{\mathrm{k}}, \Gamma) = (95\ \Omega, 1.325\ \mathrm{ms})$ $\big($i.e., $(k, \tau) = (0.24, 6.5)\big)$ for Fig. 13(b). The black solid line is the time series of $v_{\mathrm{P}}(t)$. The dotted line denotes the voltage of the operating point, $v_{\mathrm{P}}^* = 12.0$ V. The broken lines represent the edges of the safe region $v_{\mathrm{P}} \in [6.0, 19.8]$ V. The initial point $v_{\mathrm{P}}(0) = 7.6$ V is chosen from Eq. (18)

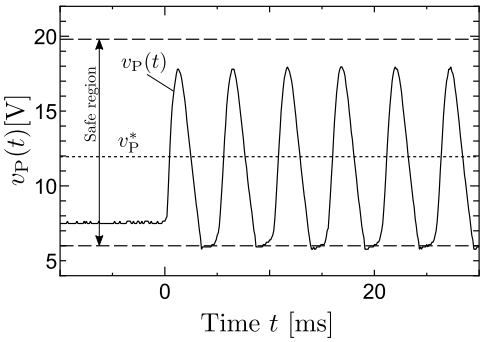

(a) $(R_{\mathrm{k}}, \Gamma) = (95\ \Omega, 0.500\ \mathrm{ms})$ $\big($i.e., $(k, \tau) = (0.24, 2.5)\big)$

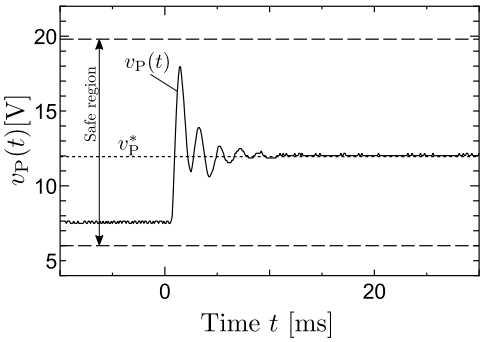

(b) $(R_{\mathrm{k}}, \Gamma) = (95\ \Omega, 1.325\ \mathrm{ms})$ $\big($i.e., $(k, \tau) = (0.24, 6.5)\big)$

Fig. 13: Time series of $v_{\mathrm{P}}(t)$ with $\boldsymbol{\Phi}_2(t)$. Dotted and broken lines represent operating point $v_{\mathrm{P}}^* = 12.0$ V and the edges of the safe region, respectively.

[7] Note that safe operation does not include the following case: the voltage $v_{\mathrm{P}}(t)$ converges to the equilibrium point but touches the edges.

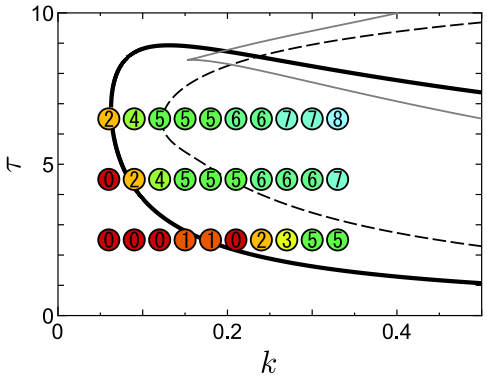

(a) with $\boldsymbol{\Phi}_1(t)$

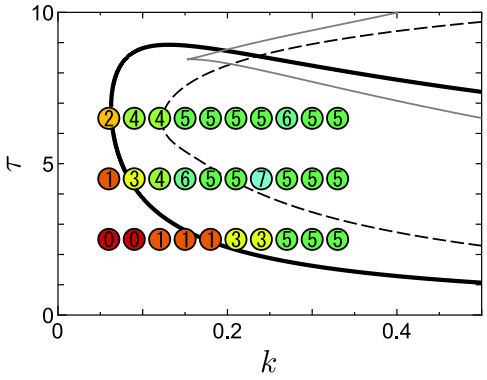

(b) with $\boldsymbol{\Phi}_2(t)$

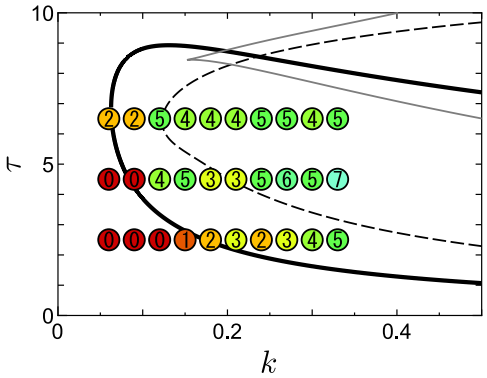

(c) with $\boldsymbol{\Phi}_3(t)$

Fig. 14: Number of initial points for safe operation (i.e., circled number) in the real DC bus circuit with DFC and bifurcation curves of system (15) in k–τ space for (a) $\boldsymbol{\Phi}_1(t)$, (b) $\boldsymbol{\Phi}_2(t)$, and (c) $\boldsymbol{\Phi}_3(t)$.

with $\boldsymbol{\Phi}_2(t)$ (see Appendix C for details of initial conditions). $v_{\mathrm{P}}(t)$ in Fig. 13(a) moves outside the safe region, whereas that in Fig. 13(b) remains in the safe region.

The basins defined above with initial functions $\boldsymbol{\Phi}_{1,2,3}(t)$ were experimentally obtained for several control parameters (k, τ). In Figs. 14(a)–14(c), a circled number indicates the number of initial points for safe operation (i.e., the number of light-blue squares). For example, the four light-blue squares shown in Fig. 12 correspond to ④ at $(k, \tau) = (0.12, 4.5)$ in Fig. 14(a).

It can be seen from Figs. 14(a)–14(c) that the following result is valid for all $\boldsymbol{\Phi}_{1,2,3}$: if (k, τ) are fixed at the right-hand side of the homoclinic bifurcation curve, the basin tends to be large. This result qualitatively agrees with the numerical results in Figs. 6 and 10. From this agreement, it can be concluded that for a type of DFC system (e.g., a DC bus circuit with DFC), the homoclinic bifurcation curve provides useful information for the design of delayed feedback controllers that make the system robust against external disturbances.

4 Discussion

This section reviews previous studies [21,26,27] on the relation of the basin to the super- and subcritical Hopf bifurcations of periodic orbits. One previous study [26] dealt with the global properties of periodic orbits stabilized by extended DFC [44]. It was shown that the basin size of the stabilized orbit depends on the type of Hopf bifurcation; the size becomes small if the stabilization occurs via a subcritical Hopf bifurcation. This result was experimentally confirmed by a non-autonomous electronic circuit (i.e., a diode resonator with an external periodic force). In addition, these results [26] were analytically investigated using bifurcation theory [27]. Furthermore, a previous study [21] dealt with the global properties of periodic orbits stabilized by a delayed feedback controller with unstable dynamics [45]. It was numerically and experimentally demonstrated that for an autonomous circuit (i.e., van der Pol oscillator), the basin size of the stabilized periodic orbit depends on the coupling function used in the controller.

The present paper examined the global properties of *equilibrium points* stabilized by *simple* (i.e., original) DFC. It was numerically shown that information on homoclinic bifurcations is useful for the design of the feedback gain and delay time of a delayed feedback controller for the normal form that has dynamics similar to that of the DC bus circuit. The numerical results were experimentally verified using a real DC bus circuit. Future work will attempt to analytically prove our numerical and experimental results.

A recent study [46] dealt with the radius of the basin of an equilibrium point in autonomous nonlinear time-delayed systems. It was shown that time-forward simulations with several simple initial functions are useful for estimating the upper bound on the radius of attraction. It was also suggested that a bifurcation analysis of the invariant sets can help one to obtain the upper bound on the radius.

5 Conclusion

This paper investigated the basin of an equilibrium point in the normal form of Bogdanov-Takens bifurcation with a simple delayed feedback controller. It was numerically shown that the basin defined with three restricted initial functions is associated with bifurcation scenarios and the unstable periodic orbit that coexists with the equilibrium point stabilized with DFC. This result indicates that for enlarging the basin, the homoclinic bifurcation curve in the control parameter space provides useful information for the design of delayed feedback controllers. In addition, the numerical results were experimentally verified using a DC bus circuit that has dynamics similar to that of the normal form.

Acknowledgements This study was supported in part by JSPS KAKENHI (18H03306 and 21H03513).

Data Availability Statement The data in this work are available from the authors on reasonable request.

Declarations

Conflicts of interest The authors declare that they have no conflicts of interest.

Appendix A: Solutions of time-delayed dynamical systems

This appendix gives a brief explanation of the solutions of autonomous time-delayed dynamical systems. For simplicity, we consider a time-delayed system with single scalar variable $x \in \mathbb{R}$ and a single constant delay $\tau \geq 0$,

$$\dot{x}(t) = f\left(x(t), x(t-\tau)\right). \tag{19}$$

The dynamics depends on both the current state $x(t)$ and the previous state $x(t-\tau)$. Therefore, a time function,

$$x(t) = \phi(t), \quad t \in [-\tau, 0], \tag{20}$$

is required as an initial condition for the time development of time-delayed system (19).

Appendix B: Saddle-node bifurcation of UPOs in a DC bus circuit with DFC

This appendix explains the bifurcation scenario that includes the saddle-node bifurcation of UPOs described by the gray lines in Fig. 9. With an increase in k from 0 for a fixed delay time $\tau \in [6.52, 10.00]$, a pair of UPOs appear at the saddle-node bifurcation curve. As an example, the bifurcation scenario with a fixed $\tau = 8.0$ is shown in Fig. 15. The top panel shows an enlarged view of the bifurcation curves in Fig. 9; the bottom panel shows a bifurcation diagram for x_1. The red symbols $\mathrm{HP_{sub}}$, HC, and SN denote the bifurcation points of the Hopf bifurcation of equilibrium point $[x^*_{1+}, x^*_{2+}]^{\mathrm{T}}$, the homoclinic bifurcation of a UPO, and the saddle-node bifurcation of UPOs, respectively.

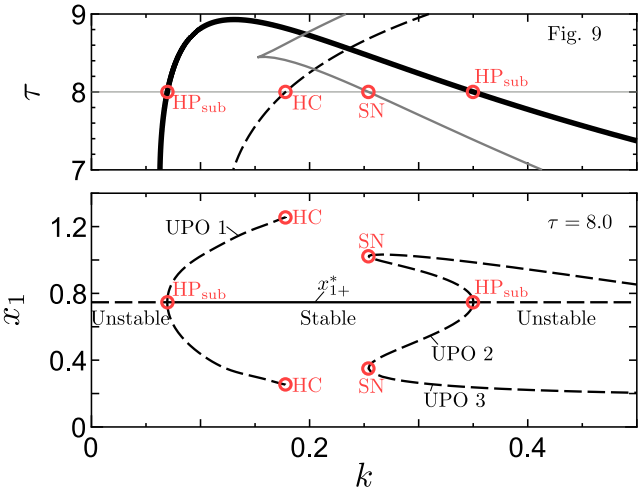

Fig. 15: Bifurcation curves (top) and bifurcation diagram (bottom) of system (15) along feedback gain k with fixed delay $\tau = 8.0$. The top panel shows an enlarged view of Fig. 9 and the bottom panel shows a bifurcation diagram for the x_1 component of $[x^*_{1+}, x^*_{2+}]^{\mathrm{T}}$ and UPOs.

We now review the bifurcation scenario in Fig. 15 with an increase in k from 0. The unstable equilibrium point $[x^*_{1+}, x^*_{2+}]^{\mathrm{T}}$ is stabilized and UPO 1 appears via a subcritical Hopf bifurcation at $k \approx 0.07$ ($\mathrm{HP_{sub}}$). With a further increase in k, UPO 1 enlarges and then disappears via the homoclinic bifurcation at $k \approx 0.18$ (HC). At $k \approx 0.25$, UPO 2 and UPO 3 are created by the saddle-node bifurcation (SN). The equilibrium point $[x^*_{1+}, x^*_{2+}]^{\mathrm{T}}$ becomes unstable and UPO 2 disappears via a subcritical Hopf bifurcation at $k \approx 0.35$ ($\mathrm{HP_{sub}}$).

Appendix C: Procedure for setting initial functions

This appendix describes an experimental procedure for setting three restricted initial functions. The implementation of the CPL and the delay unit can be found in our previous study [42]. Figure 16 shows a DC bus circuit with a delayed feedback controller. Two bipolar power

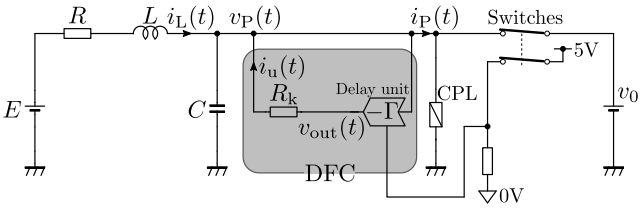

Fig. 16: DC bus circuit diagram for circuit used in our experiments. The delayed feedback controller is represented by the shaded area. E and v_0 are bipolar power supplies; two switches are opened at time $t = 0$; the delay unit (PIC18F2550) controls output voltage $v_{\rm out}(t)$ using the open/close status of the switches.

supplies[8], which can output both positive and negative currents, are used for voltage E and initial voltage v_0. The power supply that supplies v_0 is connected to the DC bus line by a switch. This switch is paired with another switch; they open and close at the same time. The lower switch is connected to a 5-V power supply. The delay unit detects whether the switch is open or closed. The delay unit is implemented using a peripheral interface controller (PIC: PIC18F2550-I/SP, Microchip Technology). The unit was modified from a previous one [42] to read the switch's open/close status and to handle a voltage range of $v_{\rm P} \in [6.0, 20.0]$ V. The output voltage $v_{\rm out}(t)$ of the delay unit can be adjusted in accordance with programs implemented in PIC.

The experimental procedure used for setting the initial functions is as follows. First, set v_0 to a voltage in the voltage set (18) and close the switches. Second, after a sufficient amount of time, open the switches at $t = 0$. Third, set the output voltage $v_{\rm out}(t)$ to

$$\boldsymbol{\Phi}_1(t): \quad v_{\rm out}(t) = v_{\rm P}(t - \Gamma) \quad t \geq 0, \tag{21}$$

$$\boldsymbol{\Phi}_2(t): \quad v_{\rm out}(t) = \begin{cases} v_{\rm P}^* & t \in [0, \Gamma) \\ v_{\rm P}(t - \Gamma) & t \geq \Gamma \end{cases}, \tag{22}$$

$$\boldsymbol{\Phi}_3(t): \quad v_{\rm out}(t) = \begin{cases} v_{\rm P}(t) & t \in [0, \Gamma) \\ v_{\rm P}(t - \Gamma) & t \geq \Gamma \end{cases}, \tag{23}$$

where $v_{\rm P}^* = 12.0$ V corresponds to the equilibrium point (i.e., the operating point) of $v_{\rm P}(t)$. We can easily see that $v_{\rm out}(t)$ in Eqs. (21) and (22) realizes the initial functions $\boldsymbol{\Phi}_1(t)$ and $\boldsymbol{\Phi}_2(t)$, respectively. $v_{\rm out}(t)$ in Eq. (23) realizes $\boldsymbol{\Phi}_3(t)$ in a shifted time scale. That is, the DC bus system starts with initial point $v_{\rm out}(0) = v_0$ and runs without control (i.e., $i_{\rm u} = 0$) from $t = 0$ to $t = \Gamma$; DFC works from $t = \Gamma$.

[8] We implemented one bipolar power supply by connecting the constant-voltage (CV) output terminal and the CV load terminal of a power supply (GPP-4323G, TEXIO). The other bipolar power supply was realized by combining the CV output (PW24-1.5AQ, TEXIO) and the CV load (PLZ164W, KIKUSUI).

References

1. Yoshida, K., Konishi, K., Hara, N.: Design of delayed feedback controller for a robust DC bus system. Proc. SICE Annual Conference, 881–885 (2018)
2. Schöll, E., Schuster, H.G. (eds.): Handbook of Chaos Control. Wiley, Weinheim, Germany (2007)
3. Pyragas, K.: Continuous control of chaos by self-controlling feedback. Phys. Lett. A **170**, 421–428 (1992)
4. Pyragas, K.: Delayed feedback control of chaos. Philos. Trans. R. Soc. A **364**, 2309–2334 (2006)
5. Hövel, P.: Control of complex nonlinear systems with delay. Springer, Berlin Heidelberg (2010)
6. Just, W., Bernard, T., Ostheimer, M., Reibold, E., Benner, H.: Mechanism of time-delayed feedback control. Phys. Rev. Lett. **78**, 203–206 (1997)
7. Hövel, P., Schöll, E.: Control of unstable steady states by time-delayed feedback methods. Phys. Rev. E **72**, 046203 (2005)
8. Brown, G., Postlethwaite, C.M., Silber, M.: Time-delayed feedback control of unstable periodic orbits near a subcritical Hopf bifurcation. Phys. D **240**, 859–871 (2011)
9. Hooton, E.W., Amann, A.: Analytical limitation for time-delayed feedback control in autonomous systems. Phys. Rev. Lett. **109**, 154101 (2012)
10. Pyragas, V., Pyragas, K.: Act-and-wait time-delayed feedback control of autonomous systems. Phys. Lett. A **382**, 574–580 (2018)
11. Čermák, J., Nechvátal, L.: On stabilization of unstable steady states of autonomous ordinary differential equations via delayed feedback controls. Phys. D **404**, 132339 (2020)
12. Ushio, T.: Limitation of delayed feedback control in nonlinear discrete-time systems. IEEE Trans. Circuits Syst. I **43**, 815–816 (1996)
13. Kokame, H., Hirata, K., Konishi, K., Mori, T.: State difference feedback for stabilizing uncertain steady states of non-linear systems. Int. J. Control **74**, 537–546 (2001)
14. Kokame, H., Hirata, K., Konishi, K., Mori, T.: Difference feedback can stabilize uncertain steady states. IEEE Trans. Autom. Control **46**, 1908–1913 (2001)
15. Cetinkaya, A., Hayakawa, T.: A sampled-data approach to Pyragas-type delayed feedback stabilization of periodic orbits. IEEE Trans. Autom. Control **64**, 3748–3755 (2019)
16. Pyragas, K., Novičenko, V.: Time-delayed feedback control design beyond the odd-number limitation. Phys. Rev. E **88**, 012903 (2013)
17. Pyragas, V., Pyragas, K.: Continuous pole placement method for time-delayed feedback controlled systems. Eur. Phys. J. B **87**, 274 (2014)
18. Ji, J.C.: Two families of super-harmonic resonances in a time-delayed nonlinear oscillator. J. Sound Vib. **349**, 299–314 (2015)
19. Shang, H., Xu, J.: Delayed feedbacks to control the fractal erosion of safe basins in a parametrically excited system. Chaos, Solitons & Fractals **41**, 1880–1896 (2009)
20. Yamasue, K., Hikihara, T.: Domain of attraction for stabilized orbits in time delayed feedback controlled Duffing systems. Phys. Rev. E **69**, 056209 (2004)

21. Höhne, K., Shirahama, H., Choe, C.U., Benner, H., Pyragas, K., Just, W.: Global properties in an experimental realization of time-delayed feedback control with an unstable control loop. Phys. Rev. Lett. **98**, 214102 (2007)
22. Wang, H., Chen, G.: On the initial function space of time-delayed systems: a time-delayed feedback control perspective. J. Frankl. Inst. **352**, 3243–3249 (2015)
23. Zheng, Y.G., Sun, J.Q.: Attractive domain of nonlinear systems with time-delayed feedback control and time-delay effects. Procedia IUTAM **22**, 51–58 (2017)
24. Leng, S., Lin, W., Kurths, J.: Basin stability in delayed dynamics. Sci. Rep. **6**, 21449 (2016)
25. Yan, Y., Xu, J., Wiercigroch, M.: Basins of attraction of the bistable region of time-delayed cutting dynamics. Phys. Rev. E **96**, 032205 (2017)
26. von Loewenich, C., Benner, H., Just, W.: Experimental relevance of global properties of time-delayed feedback control. Phys. Rev. Lett. **93**, 174101 (2004)
27. Just, W., Benner, H., von Loewenich, C.: On global properties of time-delayed feedback control: weakly nonlinear analysis. Phys. D **199**, 33–44 (2004)
28. Kuznetsov, Y.A.: Elements of applied bifurcation theory, Springer, New York (2004)
29. Singh, S., Gautam, A.R., Fulwani, D.: Constant power loads and their effects in DC distributed power systems: a review. Renew. Sustain. Energy Rev. **72**, 407–421 (2017)
30. AL-Nussairi, M.K., Bayindir, R., Padmanaban, S., Mihet-Popa, L., Siano, P.: Constant power loads (CPL) with microgrids: problem definition, stability analysis and compensation techniques. Energies **10**, 1656 (2017)
31. Hossain, E., Perez, R., Nasiri, A., Padmanaban, S.: A comprehensive review on constant power loads compensation techniques. IEEE Access **6**, 33285–33305 (2018)
32. Han, Y., Ning, X., Yang, P., Xu, L.: Review of power sharing, voltage restoration and stabilization techniques in hierarchical controlled DC microgrids. IEEE Access **7**, 149202–149223 (2019)
33. Kumar, J., Agarwal, A., Agarwal, V.: A review on overall control of DC microgrids. J. Energy Storage **21**, 113–138 (2019)
34. Fulwani, D.K., Singh, S.: Mitigation of negative impedance instabilities in DC distribution systems. Springer, Singapore (2017)
35. Engelborghs, K., Luzyanina, T., Roose, D.: Numerical bifurcation analysis of delay differential equations using DDE-BIFTOOL. ACM Trans. Math. Softw. **28**, 1–21 (2002)
36. Planas, E., Andreu, J., Gárate, J.I., Martínez de Alegría, I., Ibarra, E.: AC and DC technology in microgrids: a review. Renew. Sustain. Energy Rev. **43**, 726–749 (2015)
37. Elsayed, A.T., Mohamed, A.A., Mohammed, O.A.: DC microgrids and distribution systems: an overview. Electr. Power Syst. Res. **119**, 407–417 (2015)
38. Dragicevic, T., Lu, X., Vasquez, J.C., Guerrero, J.M.: DC microgrids—part II: a review of power architectures, applications, and standardization issues. IEEE Trans. Power Electr. **31**, 3528–3549 (2016)
39. Kumar, D., Zare, F., Ghosh, A.: DC microgrid technology: system architectures, AC grid interfaces, grounding schemes, power quality, communication networks, applications, and standardizations aspects. IEEE Access **5**, 12230–12256 (2017)
40. Prabhala, V.A., Baddipadiga, B.P., Fajri, P., Ferdowsi, M.: An overview of direct current distribution system architectures & benefits. Energies **11**, 2463 (2018)
41. Konishi, K., Sugitani, Y., Hara, N.: Analysis of a dc bus system with a nonlinear constant power load and its delayed feedback control. Phys. Rev. E **89**, 022906 (2014)
42. Yoshida, K., Konishi, K., Hara, N.: Experimental observation of destabilization in a DC bus system and its stabilization with delayed feedback control. Nonlinear Dyn. **98**, 1645–1657 (2019)
43. Konishi, K., Sugitani, Y., Hara, N.: Dynamics of dc bus networks and their stabilization by decentralized delayed feedback. Phys. Rev. E **91**, 012911 (2015)
44. Socolar, J.E.S., Sukow, D.W., Gauthier, D.J.: Stabilizing unstable periodic orbits in fast dynamical systems. Phys. Rev. E **50**, 3245–3248 (1994)
45. Pyragas, K., Pyragas, V., Benner, H.: Delayed feedback control of dynamical systems at a subcritical Hopf bifurcation. Phys. Rev. E **70**, 056222 (2004)
46. Scholl, T.H., Hagenmeyer, V., Gröll, L.: On norm-based estimations for domains of attraction in nonlinear time-delay systems. Nonlinear Dyn. **100**, 2027–2045 (2020)